Journal of Theoretical and Applied Physics (2020) 14:387–398
https://doi.org/10.1007/s40094-020-00395-0

RESEARCH

The effects of grounded electrode geometry on RF-driven cold atmospheric pressure plasma micro-jet

Davood Hassanpour[1] · **Sayyed-Jalal Pestehe**[1]

Received: 18 January 2020 / Accepted: 17 September 2020 / Published online: 6 October 2020

Abstract
With the argument that two-electrode DBD-like systems are much more operational than single-electrode systems in biomedical applications, targets sensitive to temperature and electric shock, the effects of parameters associated with the geometry of the grounded electrode such as its shape, size, and position it at the output of the atmospheric pressure RF plasma jet in two-electrode systems is investigated. By varying the position of the typical narrow ring grounded electrode on the dielectric tube toward the powered electrode, the ratio of the axial to radial electric field components depend on the externally applied potential to the plasma has been investigated and shown that the axial component of the electric field is maximized at certain position(s) of the grounded electrode. The analysis of the data indicates that there is an inverse relationship between the magnitude of the axial electric field in the plasma channel and the discharge ignition voltage, and a direct relationship with the plasma jet length. It is known that by increasing the width of the ground electrode until the full covering of dielectric, the jet length increases from the dielectric output to the neighborhood near the needle electrode, and reduces the discharge ignition threshold and consequently power consumption of the jet, but increasing its width to greater than the above values does not have a significant effect on jet output. It has also been shown that by tapering the dielectric end and fully covering it with its conical-shaped electrode, the output jet length increases and decreases its width.

Keywords Atmospheric pressure plasma jet · DBD-like · Grounded electrode geometry · Jet length · Electrode shape

Introduction

The various types of atmospheric pressure plasma jets with different structures have been reported in which they use inert gases or combine inert gases with reactive gases such as O_2 [1, 2]. Among different structures, the DBD-like structures include a powered needle electrode associated with a grounded electrode (usually ring-shaped) and single-electrode structures consist of a single powered needle or ring electrode in the absence of the grounded electrode, have operational benefits for working with radio-frequency (RF) power supplies. Figure 1 shows a schematic of these two structures.

✉ Sayyed-Jalal Pestehe
sjpest@yahoo.com

Davood Hassanpour
davood_hp@yahoo.com

[1] Advanced Plasma Laboratory, Faculty of Physics, University of Tabriz, Tabriz, Iran

As the working gas flows, such as He or Ar, through the dielectric cylinder, the gas is ionized in the vicinity of the needle electrode and a glow plasma plume exits in the downstream known as a plasma jet. These types of plasmas operate at atmospheric pressure and are classified into two major groups of cold and hot atmospheric pressure jets. Cold plasma jets have a power consumption of several tens of watts and formed jets temperature is usually close to room temperature. These types of plasma jets had numerous applications in industries including changing surface hydrophilic, surface activation of nanomaterials and catalysts [3–6], cleaning and protection of Antiquities [7]. Other uses include medical cleaning, dental canal disinfection, treating sensitive diabetic wounds, and treating cancers [8–11]. All of these applications are based on the fact that atmospheric pressure plasma jets produce a mixture of active species, ions, electrons, free radicals, and ultraviolet radiation, are transmitted by working gas flow and sheath currents, and delivered to the treated target surface, such as living tissues.

The groundless structures have shortcomings of generating relatively weaker discharge inside the dielectric tube and

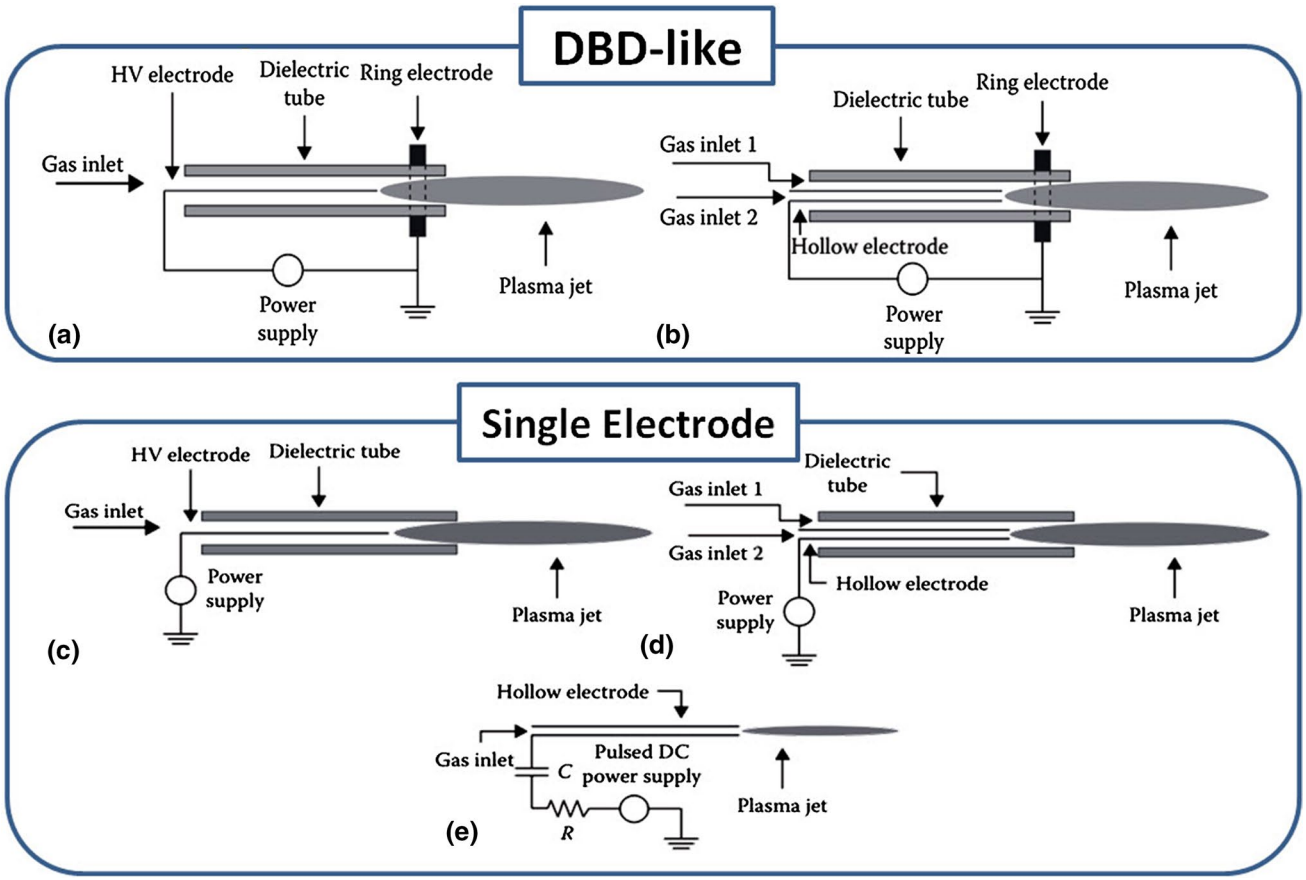

Fig. 1 DBD-like double electrode jets: **a** rod-ring **b** capillary tube-ring, and single electrode jets: **c** rod **d** metal capillary tube with Pyrex tube surrounding **e** single metal capillary tube [12]

providing low reactive species in plasma plume, because of a decreased electric field along the jet axis [12, 13]. The only central rod/hollow electrode in these systems is powered and the target, being processed, plays the rule of the ground electrode. These structures were commercialized as a small-scale electro-coagulation tool [14, 15]. This kind of systems couples plasma to the target, to some degree, and treats the target using thermal effects so they may damage it, especially the heat-sensitive tissues in medical application. Trough clinical trials, it has been shown that they can cause significantly less damage to tissues if the system's current is controlled effectively [16]. We will not consider them in this study.

Due to the physics of the problem, it can be seen that the size of the produced plasma jet may depends on the axial and radial components of the applied electric field. Based on the study of Walsh et al. [13], the existence of a grounded electrode causes the field to focus on the inter-electrodes distance (gap) and electric field lines are rather radial. They have shown that the discharge concentration in the gap increases the emitted radiation intensity of the plasma in the inter-electrodes domain and needle electrode surrounding. The length of launched plasma jet from the end of the tube is not very high. While in the absence of the grounded electrode the axial component of the electric field increases, the discharge strength inside the tube decreases that cause to increase the jet length. They have argued that a strong electric field along the plasma plume (axis) is conducive to producing longer plasma plumes and more active plasma chemistry. Lu et al. [17] in 2008 and Li et al. [18] in 2009 have reported that removing grounded electrode, discharge into the dielectric cylinder was weakened and the ionization rate of the feed gas decreased. It is noted that a strong discharge into the tube results in increased production of active species.

Given that in single-electrode systems, high probability of arcing and damage to temperature- and current-sensitive treated targets, such as cleaning and protection of antiquities and biomedical applications, have been reported [12], so for the safety of the system, two-electrode structures are preferred in such applications. Therefore, to achieve high density of active species, sufficiently long plasma jets, and also to avoid the damage caused by arcing and transition to the arc, studies on the geometry of the two-electrode structures should be

carried out to optimize the mentioned plasma parameters. In this paper, maximize of the axial component of the electric field and consequently, the optimization of the jet length and width by the change of form and location of the grounded electrode are reported.

Theoretical aspects of the system

To simulate and calculate the electric fields in the structures being studied, COMSOL Multiphysics V5.4 software was used. The AC/DC module of this software is used to simulate electric, magnetic, and electromagnetic fields in static or slow-varying modes, to design and optimize a variety of electromagnetic devices. This module has an Electrostatic toolbar that can use to calculate the parameters such as electric fields, torques, forces, potentials, and polarizations in linear and nonlinear, isotropic and anisotropic electrical systems for stationary, time-dependent and frequency domain cases (Fourier transformed space). The simulation in this module is based on the solution of Maxwell's equations and depending on the type of selected physics, may make some changes by COMSOL. Besides, depending on the chosen physics, COMSOL uses the electric charge conservation's law, and the relationships between potentials and electric and magnetic fields, such as following structural relationships:

$$\vec{D} = \varepsilon_{\mathrm{r}}\varepsilon_0\vec{E}, \quad \vec{B} = \mu_{\mathrm{r}}\mu_0\vec{H}, \quad \vec{J} = \sigma\vec{E} + \vec{J}_0 \tag{1}$$

where $\vec{J}$, σ, ε_r, ε_0 and μ are external current density, surface charge density, medium dielectric constant, free space permittivity, and medium permeability, respectively. In the AC/DC module, depending on the type of problem, one or more components among the various components, including electric and magnetic potential, electric and magnetic insulation, charge, zero current and zero field, terminal (connection to circuit), periodic boundary condition (for alternating systems), surface current, etc., can be applied to the simulation space. In addition to the mentioned boundary conditions, this module can also simulate infinite-dimensional systems.

The power source used in the experiments is an alternating sine frequency 13.54 MHz power supply, but since the determination of the axial and radial components of the electric field around the electrode is sufficient for this study, therefore, to avoid unnecessary complexity, we will benefit from the Electrostatic toolbar of the AC/DC module without diminishing the totality of the issue. This toolbar is used to calculate the electric field, electric displacement, and distribution of electric potentials in dielectric materials, with the distribution of electric charges clear. The equations examined are:

$$\nabla \cdot \vec{D} = \rho, \quad \vec{E} = -\nabla\phi \tag{2}$$

COMSOL software solves the basic electrostatic and electromagnetic equations with boundary and space conditions appropriate to problem physics, using finite element method (FEM). The three-dimensional space is divided into a large number of user-definable meshes, each of which is considered a minor element. The equations are generalized to these components and variables such as potential, electric field, and electric displacement are calculated in all space. The geometry of the device is designed in 3D using graphical tools in the software environment. The materials used in the system are called from the software database and for each component of the design a type of material with specific physical, chemical, and electrical properties is defined, and after selecting the appropriate mesh, the equations defined for the system are solved under specified boundary conditions.

Experiments setup

To investigate the effect of the geometry and position of the grounded electrode on the output jet, we use the system shown in Fig. 2a and the arrangement presented in Fig. 2b in both empirical studies and simulations. This structure consists of a powered needle electrode with outer diameter of 1.5 mm mounted on the axis of a Pyrex tube with an inner diameter and thickness of 2 mm and 1 mm, and a ring electrode connected to the ground around the Pyrex tube. RF power generator (Basafan RFG03BF) with a maximum output power of 300 W and frequency of 13.54 MHz is connected to needle electrode via L-type matching unit. The working gas in this study is argon gas with 99.999% purity flowing with 4 slm flow rate generally.

The electrical properties of the discharge were studied by measuring the voltage applied to the electrode using a high-voltage probe (Pintek HVP-39Pro). The results were recorded by a digital oscilloscope (GW Instek GDS-2304A) with a sampling rate of 2(GS/s), and a bandwidth of 300 MHz and jet dimensions were measured by digital camera. Consumed power of plasma was calculated by a 3.3 nF capacitor located between grounded electrode and earth. The stored electric charge on the capacitor, $q(t)$, may be calculated by measuring the capacitor voltage, $V_{\mathrm{C}}(t)$, from the following equation:

$$q(t) = C \cdot V_{\mathrm{C}}(t) \tag{3}$$

By plotting the Lissajous curve, capacitor charge in terms of discharge voltage ($q - V$), the area enclosed in this curve gives an estimate of the average consumed power of the plasma:

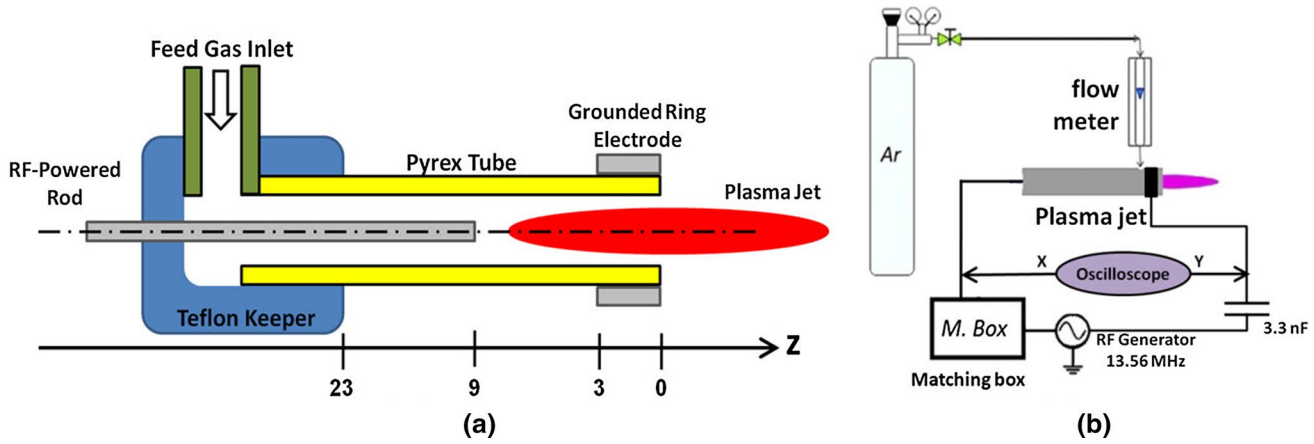

Fig. 2 The plasma jet structure studied (**a**), Schematic of the experimental setup (**b**)

$$\bar{P} = \frac{1}{T}\int_0^T V_{\mathrm{dis}}(t) I_{\mathrm{dis}}(t)\mathrm{d}t = \frac{1}{T}\int_0^T V_{\mathrm{dis}}(t).\frac{\mathrm{d}q(t)}{\mathrm{d}t}\mathrm{d}t = \frac{1}{T}S \tag{4}$$

where $I_{\mathrm{dis}}(t)$ is the current passing through the circuit consists of a plasma jet. Note that it is sufficient to derive electrical charge data, $q(t)$, from the capacitor to obtain the current passing through the circuit or the discharge current.

Results and discussion

To investigate the effect of the axial electric field on the plasma jet output generated by the two-electrode system, the arrangement shown in Fig. 2b is set and various experiments are performed. In the first experiment by changing the position of the ring electrode, in the second experiment by changing the width of the ring, and in the third experiment by changing the form of the nozzle and associated ring electrode, the output jet was evaluated and accordingly, the corresponding electric fields are extracted by the COMSOL software.

Effects of ring position on the plasma micro-jet

In the first experiment, an aluminum strip with 3 mm width was wrapped around the tube near the Pyrex tube outlet introduced in the "experiments setup" section (inner, outer diameter, and length 2, 4, and 28 mm, respectively), and at a certain distance from the outlet. A solid needle with 1.5 mm diameter and 28 mm length was chosen as the powered electrode.

Before the experiment, the potential distribution and the radial and axial components of the electric field in the mentioned structure were simulated using COMSOL software. As mentioned earlier, the purpose of the simulation here is only to achieve the ratio of the axial to radial components of the electric field in the system; therefore, calculations for electrostatic fields (DC) will not reduce the totality of the issue, consequently, the simulations have been performed using the electrostatic module in COMSOL software. Changing the position of the ring electrode position with 3 mm steps from the tube outlet backward, the discharge ignition voltage (starting the electric discharge) is measured, and the electric potential and field distributions in the discharge space as well as the space outside the Pyrex tube were calculated for the different cases presented in Figs. 3 and 4, respectively.

As it is known, the ring electrode moves away from the tube outlet and approaches the central electrode, the electric potential is concentrated in the inter-electrodes space and a significant potential drop occurs in downstream. The electric strength of argon gas is about 560 V mm^{-1}, that is if the local electric field intensity reaches this level, the argon atoms become ionized and electric discharge ignites. This discharge begins at the tip of the needle electrode as corona discharge and develops rapidly. The seed electrons create near the needle electrode in which there is a strong electric field and it can drive the plasma bullet propagation [19]. These seed electrons are placed next to needle electrode and stabilized the plasma channel. So, maybe we can say to create a plasma bullet, the rapid growth of seed electrons density in the high field region near the needle electrode is essential. Figure 4 shows points with an electric field greater than or equal to 560 V mm^{-1} in dark color, indicating the active ionization region. Specific conductivity of the discharge channel is taken 7×10^5 S m^{-1} [20]. As the ring electrode moves away from the tube outlet, the electric field is concentrated at the lateral surface of the needle electrode and the electric field distribution becomes more radial. The maximum electric field is located at the tip of the needle ($z = 11$ mm), the magnitude of which is in each case above

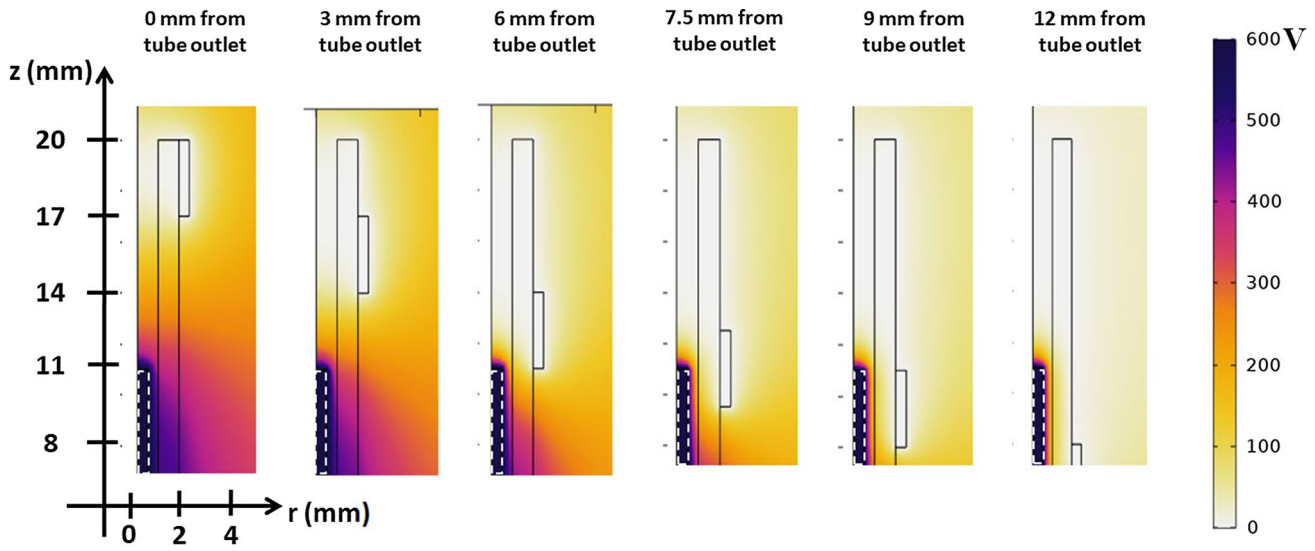

Fig. 3 Distribution of DC electrical potentials in space for different positions of the ring electrode under an applied voltage 600 V. The dashed line rectangle on the left of images is the needle electrode and the images have axial symmetry

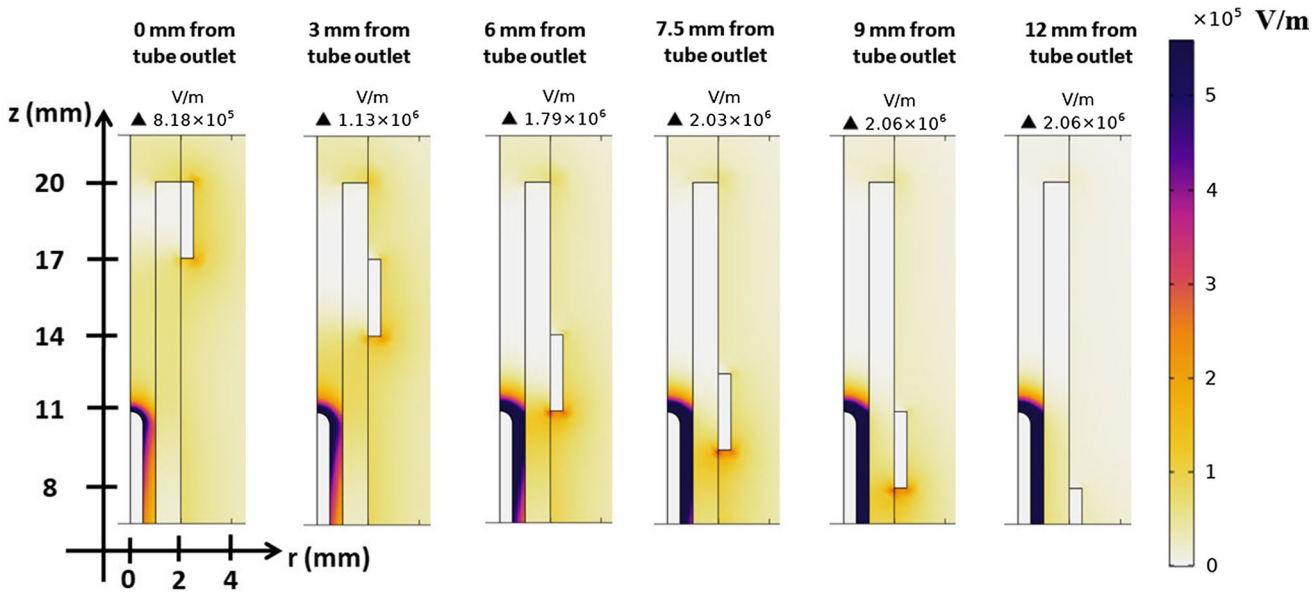

Fig. 4 Distribution of DC electrical field in discharge channel for different positions of the ring electrode under an applied voltage 600 V. The maximum field value is also stated above the images

the images, and decreases rapidly as the needle electrode moves away. Being the maximum field position at one point in all cases is in contrast to the results reported by Liu et al. in which the ANSOFT Maxwell 3D simulation software is used to simulate the DC field around a single electrode. The axial component of the electric field at the tip of the powered needle electrode by the ring electrode distance from the tip of the powered electrode is shown in Fig. 5.

We can see that the axial component of the electric field decreases by about 8 times during 1.25 mm at the tip of the needle electrode. The amount of this field component also increased with moving the ring off the end of the tube as shown in Fig. 6. The maximum electric field applied to the working gas atoms in the needle tip determines the point of the electric breakdown of the gas and its atoms ionization, which can eventually lead to an electron avalanche and cause to electric discharge. The discharge ignition voltages are measured for different positions of the ring electrode and with the maximum electric fields in the

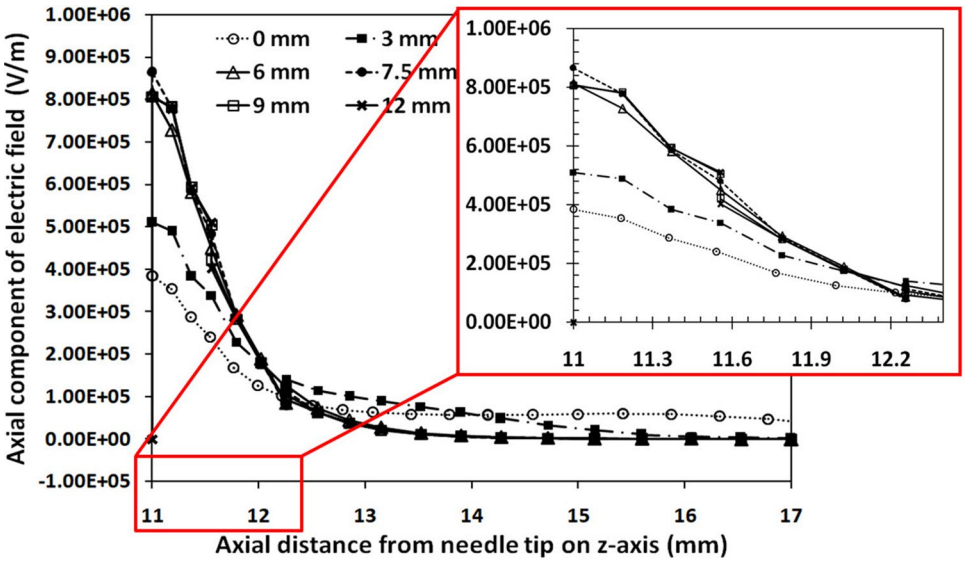

Fig. 5 The axial component of the electric field along the axis of the needle electrode (from needle tip in $z = 11$ mm) for different positions of the ring electrode (the ring distance from the tube outlet is 0, 3, 6, 7.5, 9 and 12 mm, respectively) under the operating voltage of 600 V

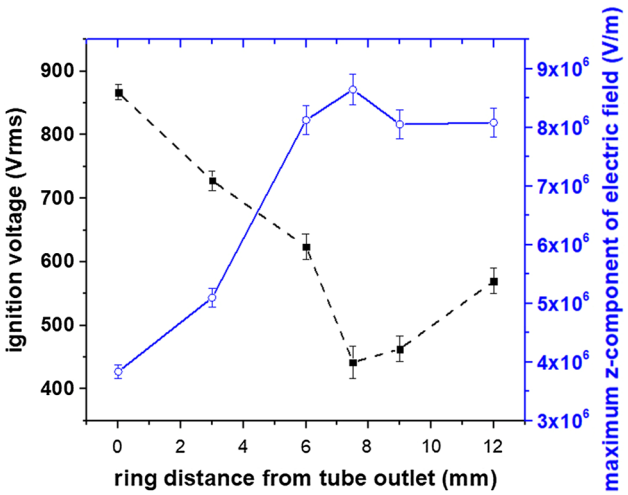

Fig. 6 Discharge ignition voltage (dash line) and maximum electric field on the jet axis (solid line) in terms of ring electrode positions

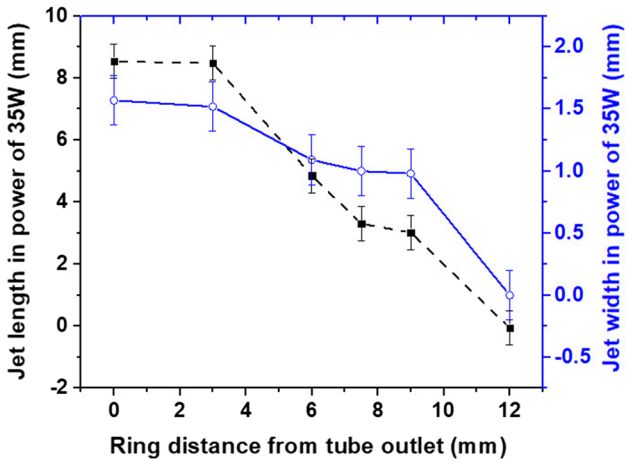

Fig. 7 The length (dash line) and width (solid line) of the plasma jet launched from Pyrex tube outlet at 35 W in different ring positions

z-direction are shown by the solid line and the dash line curves in Fig. 6, respectively.

As can be seen from this figure, the maximum electric field is increased by removing the ring from the tube outlet and approaching the needle electrode, and after passing through the tip of the needle electrode, it is slightly reduced and almost saturated. By increasing the axial component of the electric field at the tip of the needle, the voltage required for electric discharge creation and jet generation decreases, and at a minimum of 7.5 mm which corresponds to the point of contact between the ring and the tip of the needle electrode, the minimum voltage (442 V_{rms}) requires to ignite the plasma jet.

The length and width of the created plasma jet in terms of the distance of the ring from the tube outlet at applied power 35 W in Fig. 7, and an example of the waveform of discharge voltage and current is shown in Fig. 8.

As the ring electrode approaches the needle electrode, the intensity of the electric field in the inter-electrode space increases and consequently, the maximum field at the tip of the needle also increases. However, as shown in Fig. 4, as the field is increased in the inter-electrode space, the field develops at the lateral surface of the needle electrode and a saturated field is observed at the needle tip, as seen in Fig. 6. An optimum point for the ring electrode position does not appear, but as shown in Fig. 7, when the ring is closer to the tube outlet, the length of the plasma jet is longer, although the discharge ignition threshold voltage is higher in this case. So, there has to be a balance between these two factors.

As the ring electrode moves away from the tube outlet, the jet length and width decrease (Fig. 7). This decrease is

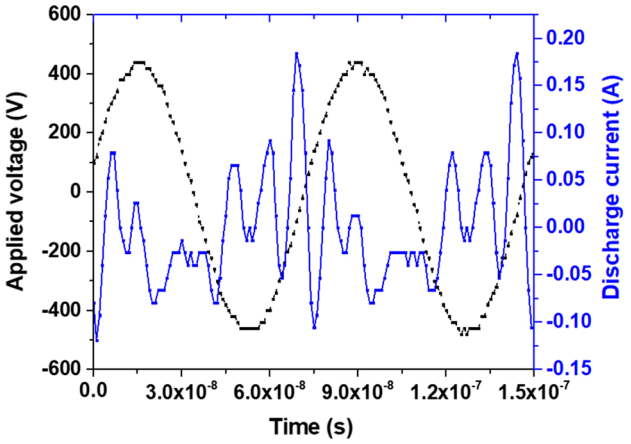

Fig. 8 The waveform of discharge voltage (dash line) and current (solid line) when the ring electrode is located at the tube outlet (0 mm from the tube outlet) and applied power of 35 W with a voltage of 345 V_{rms}

due to the weakening of the electric field in the tube outlet. In fact, by transferring the ring electrode to the needle electrode, the intensity of the electric field is concentrated in inter-electrodes space, and the field intensity in the jet launching region decreases. In fact, with this transferring, the radial component of the field gradually becomes stronger and the axial component is weakened. Thus, although the radial component strengthens, resulting in earlier ignition discharge at lower voltages, due to the weakening of the axial component of the field, it is expected that the produced plasma jet length will be reduced, which is shown in Fig. 7. It is therefore found that for longer jet lengths, the ring electrode should be as close as possible to the tube outlet. On the other hand, approaching the ring to the needle electrode also results in lower voltages for discharge ignition, so the proximity of the two electrodes to each other is also important in the design of these jets.

Before the discharge created, both the voltage and current waveforms are sinusoidal, and due to the capacitive load of the system, the current has a phase difference of about 90 degrees concerning the voltage, and the Lissajous curve discussed above also appears oval. As the discharge occurred and the plasma generated, as shown in Fig. 8, distortions appear on the current waveform and the Lissajous curve gets out of its elliptical shape (Fig. 9).

For the optimum position of the 3 mm ring electrode (7.5 mm from the tube outlet, where the needle tip is located exactly in the middle of the ring electrode), with feed gas flow rate of 4 slm by applying voltage changes between the two electrodes, the jet length and width, as well as the Lissajous curve, which is a measure of the average consumed power of the plasma, have been measured. In Fig. 9, a sample of the Lissajous curves for two effective voltages of 300 and 385 V (30 and 50 W applied power) and the produced jet shapes are shown.

It is clear that as the voltage increases; the area inside the curve also increases, indicating an increase in the average consumed power of the plasma jet. In these conditions, the argon gas flow rate is 4 slm, and the operating voltage amplitudes are 420 V and 540 V by 30 W and 50 W applied power. The calculated power consumed by this method (Lissajous enclosed area) is 4.57 W and 5.85 W, respectively. The length and width of the generated jet under different voltages are shown in Fig. 10.

As the applied voltage increases, the resulting electric field increases and in addition to increasing the power consumption of the plasma jet, the stability and uniformity

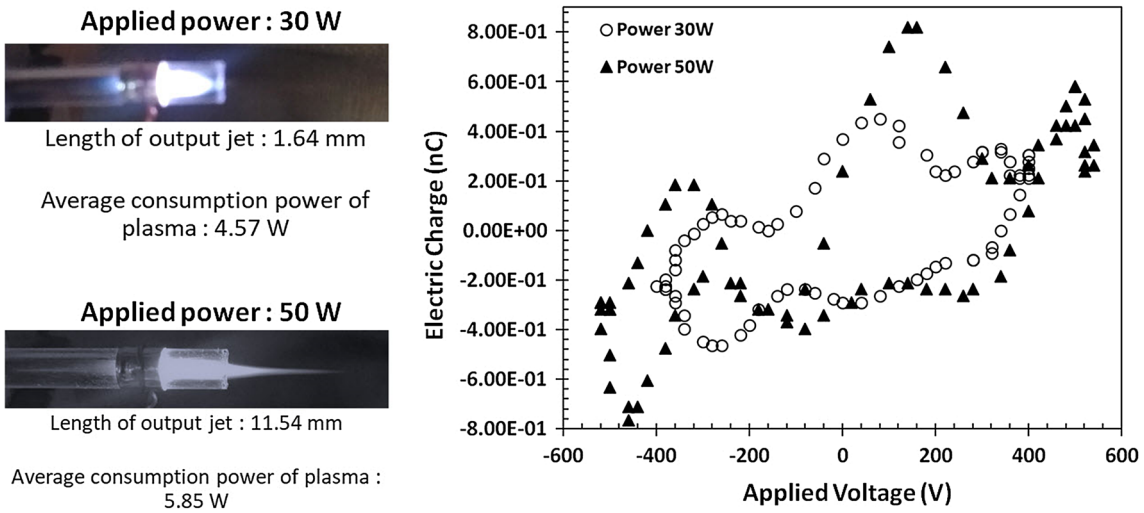

Fig. 9 The $q - V$ Lissajous curve for two effective voltages of 300 and 385 V with feed gas flow rate of 4 slm and image of the jet launched from tube outlet in each case

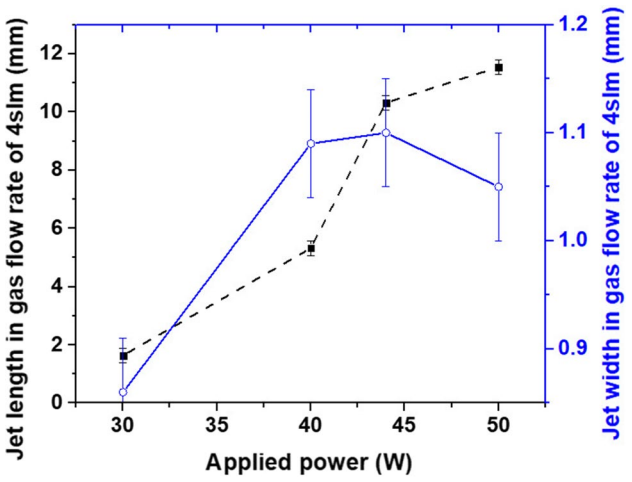

Fig. 10 Length (dash line) and width (solid line) of the produced jet in term of different applied powers in gas flow rate of 4 slm

of the formed plasma are also increased. The voltage can be increased to the extent that the operating regime of the plasma jet does not change (breakdown in a dielectric barrier and transition to electric arc). By changing the operating regime and switching to the arc mode, the plasma temperature rises rapidly and also destroys the powered electrode [21]. Increasing the voltage increases the plasma jet length and decreases the plasma width after the initial increase.

If we consider the voltage-to-current (peak-to-peak) ratio of the plasma as a measure of the real resistance of the system, according to Fig. 11, as the voltage increases that increases the jet length, the resistance of the plasma medium decreases, which may reflect the increase in ionization in the plasma. The plasma efficiency, which is the ratio of average consumed power to applied power, decreases with increasing voltage.

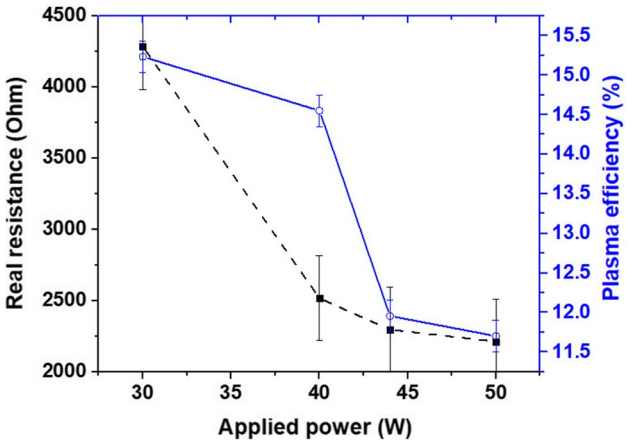

Fig. 11 Real resistance scale (dash line) and the plasma efficiency (solid line) at different applied powers

The feed gas flows inside the Pyrex tube at low flow rates under the laminar regime and at higher flow rates under turbulent regime [22]. The scale used to distinguish between these two modes is the Reynolds number, which is defined as follows:

$$\mathrm{Re} = \frac{u D_{\mathrm{H}}}{\upsilon} \tag{5}$$

where u, D_{H} and υ are, respectively, the mean speed of the fluid (m s^{-1}), the hydraulic diameter of the pipe (m) and kinematic viscosity of the fluid (m s^{-1}) which is dependent on the pressure and temperature. In laminar flow, streams move in parallel layers (lamina) that present a steady macroscopic mixing without intersection between each other, but in the turbulent flow that occurs in flow rates beyond a certain critical value, the fluid motion is irregular and turbulent [23]. According to Jin's 2013 studies [24], the plasma jet lengths of He, Ne, and Ar inside the Pyrex tube increase with increasing Reynolds number from zero to about 2000 under the laminar state regime; however, as the Reynolds number increases to values above 2000, the fluid is transitioning from a laminar regime to a turbulent regime and the jet length begins to decrease. In the transition stage that extends up to about Reynolds number 4000, the fluid flow is unstable and the fluid turbulence is on the verge of emergence that in Reynolds numbers beyond this we will have only the turbulent regime. Figure 12 shows the dependence of the length and width of the produced plasma jet on the feed gas flow rate. We can see that the launched jet length has a maximum at 4 slm, which at flow rates below that, the direct relationship between the jet length and the gas flow rate, and states that the gas flow is laminar. At flow rates exceeding this value, the jet length decreases and enters the

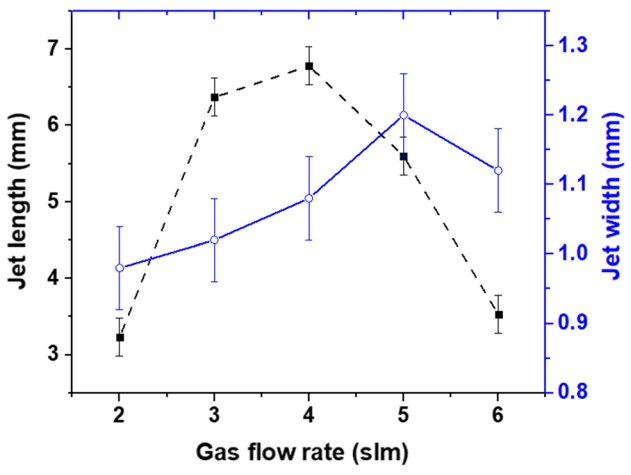

Fig. 12 Length (dash line) and width (solid line) of the plasma jet in tube outlet with applying 40 W (voltage of 350 V_{rms}) in different argon gas flow rates

laminar-to-turbulent transition phase. Also, the maximum jet width is in the position of reducing its length.

Changing the ring width to the complete tube covering

It is shown in Fig. 7 that the ring should be as close as possible to the tube outlet; on the other hand, as the ring approached the tip of the needle electrode, the field intensity at the tip of the needle was amplified and the ignition voltage decreased. Therefore, at this stage of the experiments, we increase the width of the ring electrode starting at the tube outlet to fully cover the surface of the tube. In each case, we measure the applied power and voltage to the discharge ignition and the output jet length at 35 W (Fig. 13). The distribution of the electric field and the extent of the active ionization zone in the discharge channel are shown in Fig. 14.

In Fig. 13a, as in Fig. 6, increasing the thickness of the ring electrode from the tube outlet to the contact point of the ring with and needle electrodes, cause to increase the maximum electric field and saturate after reaching the needle tip position. The discharge ignition voltage reversely depends on the axial field intensity. The jet length launched from the tube is in good agreement with the maximum axial electric field.

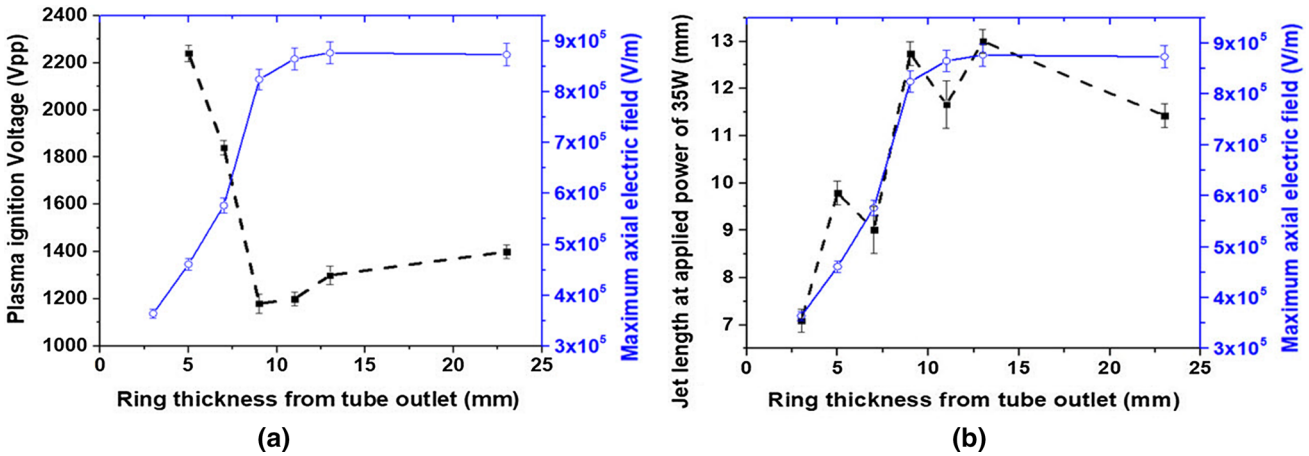

Fig. 13 The discharge ignition voltage (**a**) and the length (**b**) of the jet launched from the tube outlet compared with the maximum axial electric field (solid line) for the different thicknesses of the grounded ring electrode

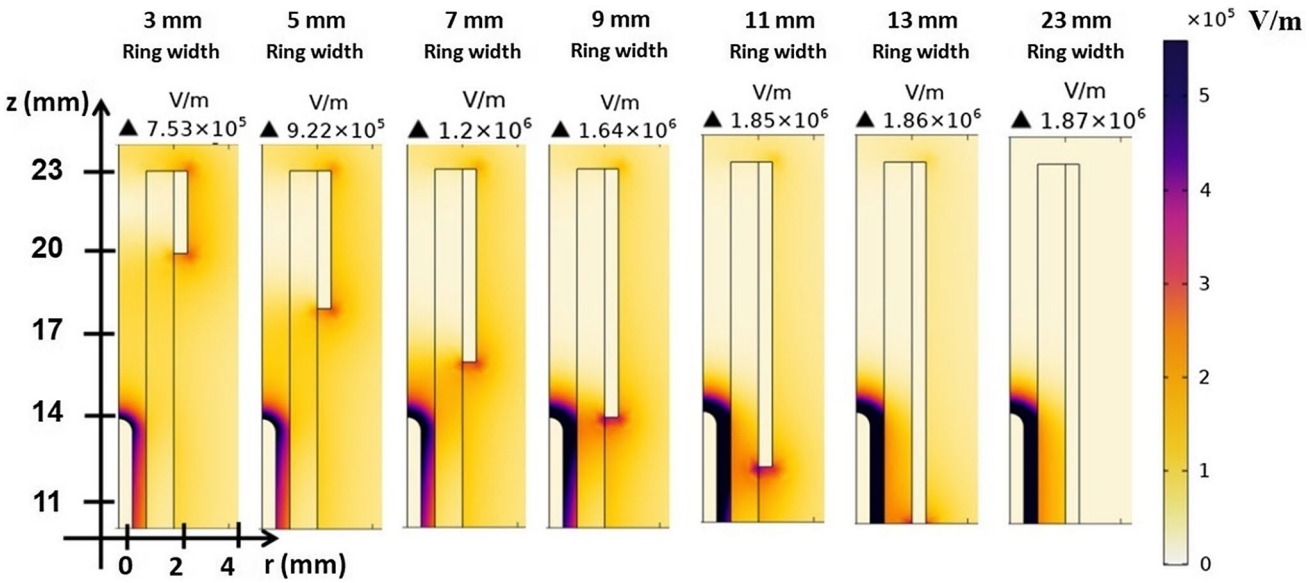

Fig. 14 Distribution of the electric field intensity in the discharge channel

Grounded electrode shape

It was largely found that increasing the length of the grounded electrode and completely covering the outer surface of the Pyrex tube is very effective to increase the axial electric field as well as to trap the electric field lines in order not to get out of the tube. Therefore, in this step, we consider the three distinct structures shown in Fig. 15 to study the effects of the grounded electrode shape on the launched plasma jet and the systems' output measure under identical operating conditions. The system of Fig. 15a has considered being in the best position of the ring electrode, is reconsidered to show the reproducibility of the previous results, and to compare its results with the conical-ended system.

In previous experiments, when the grounded electrode covers the entire dielectric surface, during the discharge ignition occurring at high power, due to high heat generation, the dielectric Pyrex was shocked through ignition it lost its character. In these structures, refractory Teflon (PTFE) dielectric has been used instead of glass in order to avoid the electric breakdown in the Pyrex tube and its destruction; because the Teflon dielectric coefficient, electric strength, specific bulk, resistivity, and insulation loss coefficient are $\varepsilon_r = 2.1$, $< 60\,\text{kV mm}^{-1}$, $> 10^{15}\Omega\,\text{cm}$, and 2×10^{-4}, respectively, whereas for Pyrex glass these numbers are $\varepsilon_r \geq 5$, $14\,\text{kV mm}^{-1}$, $4\times10^{6}\,\Omega\,\text{cm}$ and 4×10^{-2}, respectively [25]. This means that Teflon's stability to the arcing is much higher than that of Pyrex, and its reliability is higher. The Teflon dielectric in all three structures with inner and outer diameters of 3 mm and 5 mm and length of 27 mm was turned from Teflon rod. In the third structure, the Teflon dielectric bottom is turned in form of a cone with vertex angle of 25° and had a 2 mm output aperture. The grounded electrodes in these structures are aluminum, and are, respectively, (a) a ring in 3 mm width and 0.2 m thickness in the best position based on previous measurements; (b) a cylinder in 0.2 mm thickness that fully covers the surface of the dielectric tube, and (c) a cylinder in 1 mm thickness with conical-ended shape that is in full contact with the Teflon dielectric.

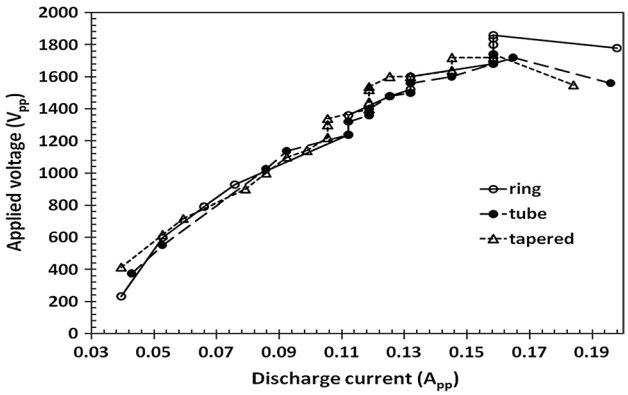

Fig. 16 The characteristic curve for the three structures shown in Fig. 15

The characteristic curves (I–V) of these structures are shown in Fig. 16. The discharge current in these structures is extracted from the electric charge transmitted through a mica capacitor with 3.3 nF capacitance, which its electrical capacity is chosen to be large enough compared to the system's electrical capacity in silent mode (about 1.6 nF measured by RLC-meter model: KDK KC–605 made by: Kokuyo Electronic Co. LTD.) [26]. It can be seen that the amplitude of the breakdown voltage and the current passing through the circuit in the breakdown phase for these three structures are as follows: 930 V and 79.2 mA for the ring system, 860 V and 82.4 mA for the cylindrical system, and 870 V and 79.2 mA for the conical-end system.

The output of the simulation software for these three structures is shown in Fig. 17. As shown in the images, the maximum amount of electric field at the tip of the needle electrode is also directly related to the maximum field and the discharge ignition voltage (Fig. 16). The field intensities in the conical-ended and cylindrical structures are approximately equal and there is a considerable difference between them and the ring structure.

The power, ignition voltage, and discharge currents in these three systems for argon feed gas with volume flow rate 5 slm are given in Table 1. By examining the data in Table 1 and Fig. 18, which show the Lissajous curve of these three

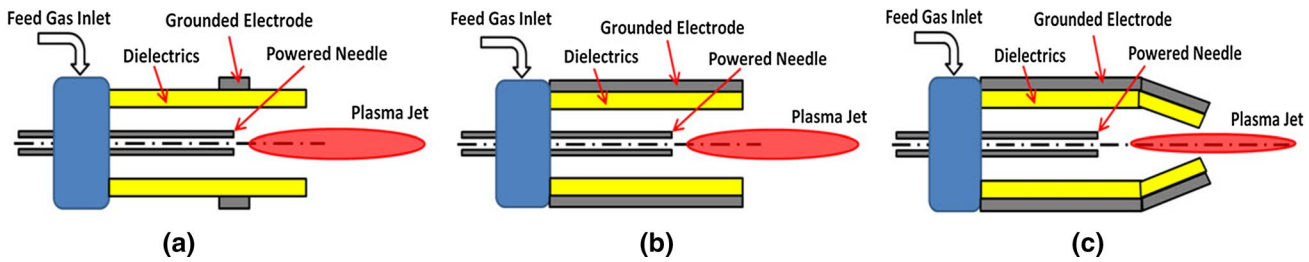

Fig. 15 Three distinct structures of the grounded electrode: **a** ring, **b** cylinder, **c** conical ended

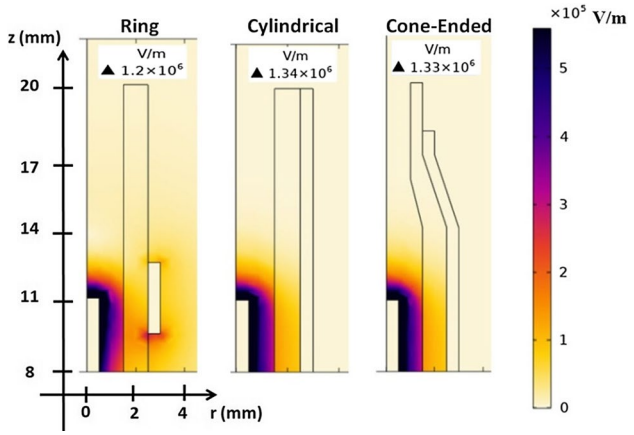

Fig. 17 Distribution of the electric field in the electrode space in the three structures shown in Fig. 15

structures, it can be seen that the power required for the discharge ignition in the cone-shaped system is less than that of the other structures.

The average power consumption of the plasma using a capacitor located in the ground electrode circuit and using the charge–voltage (q–V) Lissajous curve shown in Fig. 18 and Eqs. (3) and (4) is measured, and with the produced jet dimensions measured under the same conditions (gas flow rate 5 slm, applied voltage 360 V_{rms}, and operating frequency 13.56 MHz) are presented in Table 2. From these data, it can be deduced that the cone-ended system can be preferred over others.

Along with maximum of the electric field intensity in Fig. 17 and the discharge ignition voltage in Fig. 16, the plasma jet length measurement also shows that the conical-ended and cylindrical structures have the maximum field, ignition voltage, and approximately the same jet length; however, the jet length in the conical-ended structure is more than the cylindrical structure, which may be due to the narrowing of the ionizing gas outlet and the change in local flow rate at that point. From these data, it can be deduced that the conical-ended system can be preferred over others and should therefore be considered in the design of plasma jets.

Conclusions

For reasons such as the weakening of discharge due to the reduced ionization rate of the feed gas, the reduction of active species production and also to prevent damage to the treated targets stated in the introduction of the this paper, to work in RF mode, the two-electrode systems called DBD-like structures are preferred. Given the differences in the various structures employed by different authors, it was expected that there would be a relationship between the components of the electric field (axial and radial) governing the discharge and the produced jet. The results of the COMSOL simulations and practical measurements show that there is an inverse relationship between the axial electric field in the plasma channel and the plasma ignition voltage. Also, the stronger the axial components of the electric field occur the faster the electric discharge and consequently plasma jet produces sooner. Besides, with the increase in this component of the field, the length of the formed plasma jet is also longer. Approaching the grounded electrode to the needle electrode reduces the inter-electrode space and confines the field lines to a smaller space and increases the electric field intensity near the needle electrode. It was shown that the electric field develops at the lateral surface of the needle electrode and its axial component less develops than the radial component. However, the development of the radial

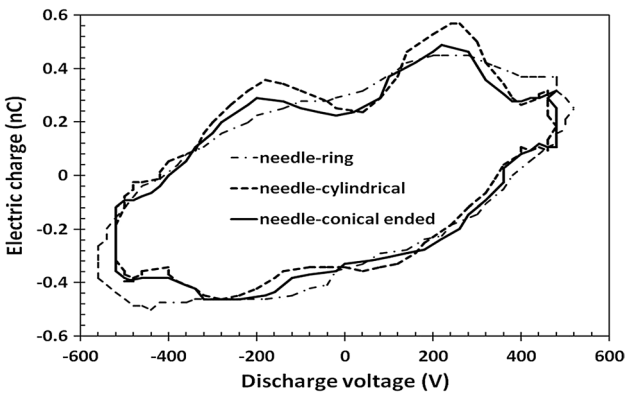

Fig. 18 Lissajous curve for the structures shown in Fig. 15

Table 1 The ignition and post-ignition voltages and currents for the three structures shown in Fig. 15

Structures	Discharge ignition power (W)	Voltage amplitude (V) before/after discharge	Current amplitude (mA) before/after discharge
Needle-ring	116	930/890	79.2/99
Needle-cylinder	99	860/780	82.4/98
Cone-ended cylinder	98	870/775	79.2/92

Table 2 The outlet jet dimensions, discharge current and average consumed plasma power

Structures	Jet length (mm)	Jet width (mm)	Average consumed power (W)	Current amplitude (mA)
Needle-ring	3.75	1.83	7.93	56.10
Needle-cylinder	7.38	2.11	7.48	95.70
Cone-ended cylinder	7.69	1.82	6.72	75.90

components and the concentration of field lines between the electrodes facilitate the discharge ignition, although it reduces the plasma jet length. This decrease in the length is due to the weakening of the electric field in the tube outlet. At the contact point of the ring electrode with the needle electrode tip, the lowest voltage is required for the discharge ignition. This is also true when the width of the ground electrode is increased. It was shown that the shape of the grounded electrode is also effective in the plasma jet output and a structure with conical-ended shape has the longest produced jet.

References

1. Liu, F., Sun, P., Bai, N., Tian, Y., Zhou, H., Wei, S., Zhou, Y., Zhang, J., Zhu, W., Becker, K., Fang, J.: Inactivation of bacteria in an aqueous environment by a direct-current, cold-atmospheric-pressure air plasma micro-jet. Plasma Proc. Polym. **7**, 231–236 (2010)
2. Babayan, S.E., Jeong, J.Y., Tu, V.J., Park, J., Selwyn, G.S., Hicks, R.F.: Deposition of silicon dioxide films with an atmospheric pressure plasma jet. Plasma Source Sci. Technol. **7**(3), 286–288 (1998)
3. Cheng, C., Liye, Z., Zhan, R.: Surface modification of polymer fiber by the new atmospheric pressure cold plasma. Surf. Coat. Technol. **200**, 6659–6665 (2006)
4. Chen, G., Chen, S., Zhou, M., Feng, W., Gu, W., Yang, S.: The preliminary discharge characterization of a noble APGD plume and its application in organic contaminated degradation. Plasma Sour. Sci. Technol. **15**, 603–608 (2006)
5. Ha, H., Moon, B.K., Horiuchi, T., Inushima, T., Ishiwara, H., Koinuma, H.: Structure and electric properties of TiO_2 films prepared by cold plasma torch under atmospheric pressure. Mater. Sci. Eng., B **41**(1), 143–147 (1996)
6. Liu, X., Chen, F., Huang, S., Yang, X., Lu, Y., Zhou, W., Xu, W.: Characteristic and application study of cold atmospheric-pressure nitrogen plasma jet. IEEE Trans. Plasma Sci. **43**(6), 1959–1968 (2015)
7. Klíma, M., Slavíček, P., Šíra, M., Čižmár, T., Vaněk, P.: HF plasma pencil and DC diaphragm discharge in liquids—diagnostics and applications. J. Czech. Phys. **56**, B1051–B1056 (2006)
8. Sun, P., Pan, J., Tian, Y., Bai, N., Wu, H., Wang, L., Yu, C., Zhang, J., Zhu, W.: Tooth whitening with hydrogen peroxide assisted by a direct-current cold atmospheric-pressure air plasma micro-jet. IEEE Trans. Plasma Sci. **38**(8), 1892–1896 (2010)
9. Jiang, C., Chen, M., Gorur, A., Schaudinn, C., Jaramillo, D.E., Costerton, J.W., Sedghizadeh, P.P., Vernier, P.T., Gundersen, M.A.: Nanosecond pulsed plasma dental probe. Plasma Process. Polym. **6**, 479–483 (2009)
10. Pesnel, S., Vandamme, M., Lerondel, S., Le Pape, A., Robert, E., Dozias, S., Barbosa, E., Pouvesle, J.: Antitumor effect of plasma exposure: preliminary results in a mouse model. In: Proceedings of the 2nd International Conference on Plasma Medicine. San Antonio, TX (2009)
11. Lu, X., Keidar, M., Laroussi, M., Choi, E., Szili, E.J., Ostrikov, K.: Transcutaneous plasma stress: from soft-matter models to living tissues. Mater. Sci. Eng., R **138**, 36–59 (2019)
12. Lu, X., Laroussi, M., Puech, V.: On atmospheric-pressure non-equilibrium plasma jets and plasma bullets. Plasma Sour. Sci. Technol. **21**, 034005 (2012)
13. Walsh, J.L., Kong, M.G.: Contrasting characteristics of linear-field and cross-field atmospheric plasma jets. Appl. Phys. Lett. **93**(11), 111501 (2008)
14. Leveille, V., Coulombe, S.: Design and preliminary characterization of a miniature pulsed RF APGD torch with downstream injection of the source of reactive species, *Plasma Sour*. Sci. Technol. **14**, 467–476 (2005)
15. Storek, D., Grund, K.E., Gronbach, G., Farin, G., Becker, H.D.: Endoscopic argon gas coagulation--initial clinical experiences. Z. Gastroenterol. **31**, 675–679 (1993). **(in German)**
16. Stoffels, E., Kief, I.E., Sladek, R.E.J.: Superficial treatment of mammalian cells using plasma needle. J. Phys. D Appl. Phys. **36**(23), 2908–2913 (2003)
17. Lu, X., Jiang, Z., Xiong, Q., Tang, Z., Pan, Y.: A single electrode room-temperature plasma jet device for biomedical applications. Appl. Phys. Lett. **92**, 151504 (2008)
18. Li, Q., Li, J.T., Zhu, W.C., Zhu, X.M., Pu, Y.K.: Effects of gas flow rate on the length of atmospheric pressure non-equilibrium plasma jets. Appl. Phys. Lett. **95**(14), 141502 (2009)
19. Lu, X., Ostrikov, K.: Guided ionization waves: the physics of repeatability. Appl. Phys. Rev. **5**, 031102 (2018)
20. Liu, W., Li, Z., Zhao, L., Zheng, Q., Ma, C.: Study on formation mechanism of atmospheric pressure glow discharge air plasma jet. Phys. Plasmas **25**, 083505 (2018)
21. Walsh, J.L., Iza, F., Janson, N.B., Law, V.J., Kong, M.G.: Three distinct modes in a cold atmospheric pressure plasma jet. J. Phys. D Appl. Phys. **43**(7), 75201 (2010)
22. Yan, W., Economou, D.J.: Gas flow rate dependence of the discharge characteristics of a helium atmospheric pressure plasma jet interacting with a substrate. J. Phys. D Appl. Phys. **50**, 415205 (2017)
23. Stoffels, E., Gonzalvo, Y.A., Whitmore, T.D., Seymour, D.L., Rees, J.A.: A plasma needle generates nitric oxide. Plasma Sour. Sci. Technol. **15**, 501–506 (2006)
24. Jin, D.J., Uhm, H.S., Cho, G.: Influence of the gas-flow Reynolds number on a plasma column in a glass tube. Phys. Plasmas **20**(8), 083513 (2013)
25. Haynes, W.M. (ed.): CRC Handbook of Chemistry and Physics. Taylor & Francis Group, Cambridge (2013)
26. Ashpis, D.E., Laun, M.C., Griebeler, E.L.: Progress toward accurate measurement of dielectric barrier discharge plasma actuator power. J. AIAA **55**(7), 2254–2268 (2017)